ORIGINAL PAPER

WS$_2$ quantum dots-MnO$_2$ nanosheet system for use in ratiometric fluorometric/scattered light detection of glutathione

Fanyong Yan[1] · Zhonghui Sun[1] · Jinxia Xu[1] · Hejing Li[1] · Yuyang Zhang[1]

Abstract

Based on WS$_2$ quantum dots (QDs) as fluorescent signals and MnO$_2$ nanosheets as second-order scattering (SOS) signals, a combination of fluorescence and scattered light was used to construct a ratio sensing platform for glutathione (GSH) detection. When MnO$_2$ nanosheets are added to WS$_2$ QDs, the fluorescence of WS$_2$ QDs is quenched by MnO$_2$ nanosheets through IFE. Large-sized MnO$_2$ nanosheets increase the SOS of the system and gradually approach the fluorescence. After adding GSH to WS$_2$ QDs-MnO$_2$, the MnO$_2$ nanosheets were decomposed into Mn^{2+}. The disappearance of the characteristic absorption peak of the MnO$_2$ nanosheets suppressed the IFE to WS$_2$ QDs, resulting in the fluorescence recovery of WS$_2$ QDs. The reduction in size of MnO$_2$ nanosheets after decomposition results in a decrease in the SOS of the system. Therefore, the ratio detection of GSH is obtained through the fluorescence and SOS dual signal response. Under optimal experimental conditions, the value of F_{406}/S_{648} is linearly related to the GSH concentration in the range 0 to 60 μM, and the limit of detection (LOD) of GSH is 0.12 μM. In addition, the system is also used for the determination of GSH in real water samples and human serum, with good analytical results.

Introduction

Glutathione (GSH) is an important non-protein thiol compound in animal and plant cells [1, 2]. GSH plays a very important role in scavenging free radicals, detoxifying, maintaining DNA biosynthesis, maintaining intracellular redox homeostasis, and participating in metabolism [3–5]. Abnormal levels of GSH are associated with many diseases, such as cancer, diabetes, Alzheimer's disease, and human immunodeficiency virus (HIV) [6–8]. The establishment of accurate,

rapid, and sensitive methods for the detection of GSH has important biological and clinical significance. At present, common methods for detecting GSH mainly include colorimetry, electrochemical methods, high-performance liquid chromatography (HPLC), fluorescence spectrometry, and mass spectroscopy [9, 10]. Among them, fluorescence spectroscopy has the advantages of simple operation, instant detection, high sensitivity, and good selectivity [11]. Compared with a single fluorescence response signal, the ratio fluorescence method has the advantage of effectively overcoming the positive and negative errors caused by various interferences (such as environmental changes, sample background signals, and instrument changes), so the ratio fluorescence method with self-calibration characteristics has attracted more and more attention [12–16].

WS$_2$ is a well-known transition metal disulfide with a graphene-like two-dimensional layered structure. Due to the typical small size effect and boundary effect, WS$_2$ QDs have unique optical properties and good biocompatibility [17–19]. WS$_2$ QDs are widely used in the fields of catalysis, optical imaging, fluorescence sensing, and batteries due to their good light stability, easy preparation, low cost, and low toxicity [20,

✉ Fanyong Yan
yanfanyong@tiangong.edu.cn

1 State Key Laboratory of Separation Membranes and Membrane Processes/National Center for International Joint Research on Separation Membranes, School of Chemistry and Chemical Engineering, Tiangong University, Tianjin 300387, People's Republic of China

⌷ Springer

21]. MnO$_2$ nanosheet is a new class of two-dimensional nanomaterials, which has extensive UV-Vis absorption and high specific surface area, so it is an excellent fluorescence quencher and effective scatterer [22, 23]. MnO$_2$ nanosheets can also be reduced to Mn^{2+} by GSH without harming the environment or human health and have good biocompatibility [24, 25]. These characteristics have caused MnO$_2$ nanosheets to attract widespread attention in the field of building new sensors [26, 27]. Under incident light, the larger MnO$_2$ nanosheets show two scattering peaks in the fluorescence spectrum. First-order scattering (FOS) is a scattering peak at the incident wavelength; second-order scattering (SOS) is a scattering peak at twice the wavelength of the incident light. In general, the intensity of scattered light is related to the size and number of scatterers in solution [28–30]. Fraunhofer's single slit diffraction law [31] shows that FOS is much stronger than SOS. And we observe that the peak intensities of FOS and fluorescence are quite different, while the peak intensities of SOS and fluorescence are relatively close. Therefore, we combined two different optical signals, fluorescence and SOS, and recorded changes in the fluorescence quenching ability and scattered light intensity of the MnO$_2$ nanosheets caused by GSH induction on a fluorometer to obtain high sensitivity and accurate detection.

In this paper, a ratio method for GSH detection was established by combining the fluorescence of WS$_2$ QDs with the SOS of MnO$_2$ nanosheets (Scheme 1). After adding MnO$_2$ nanosheets to WS$_2$ QDs, the fluorescence of WS$_2$ QDs will be quenched by MnO$_2$ nanosheets through IFE, and SOS is enhanced due to the increase of scatterers (the intensity of SOS is close to the fluorescence before GSH was added). With the addition of GSH, the MnO$_2$ nanosheets were reduced to Mn^{2+}, which caused the fluorescence of WS$_2$ QDs to recover and the SOS of the scatterer to decrease. Therefore, the ratio detection of GSH can be realized by the WS$_2$ QDs-MnO$_2$ system. In addition, the proportional system has also been successfully used for the quantitative analysis of GSH in real water samples and human

serum, which proves that the WS$_2$ QDs-MnO$_2$ system has great application potential in GSH sensing.

Experimental

Materials and apparatus

Sodium tungstate, sodium dodecyl benzene sulfonate (SDBS), and KMnO$_4$ were obtained from Macklin Biochemical Co., Ltd. (Shanghai, China). Homocysteine (Hcy), L-cysteine (Cys), serine (Ser), tyrosine (Tyr), glycine (Gly), histidine (His), L-glutathione (GSH), glucose, galactose, and bovine serum albumin (BSA) were purchased from Blue Season Technology Development Co., Ltd. (Shanghai, China). NaCl and other metal salts were purchased from Damao Chemical Reagent Factory (Tianjin, China). Deionized water was used to prepare all solutions. All chemicals and reagents were of AR grade and used as received.

Mettler Toledo pH meter was used to measure the pH values of solutions. The UV-Vis absorption spectra were made on a TU-1901 spectrometer (Purkinje, General). The fluorescence spectra were measured on a F-380 fluorescence spectrophotometer (Gangdong scientific and technological development). Fourier transform infrared (FT-IR) was performed on a TENSOR37 (China) spectrometer. X-ray photoelectron spectroscopy (XPS) analyses were carried out on an ESCALab220i-XL spectrometer. The X-ray diffraction (XRD) patterns were given from Bede-D1 X-ray diffractometer. Transmission electron microscopy (TEM) was measured on a Tecnai F20 microscope. Fluorescence lifetimes were recorded on FLS 980 (UK).

Synthesis of WS$_2$ QDs

The synthesis method of WS$_2$ QDs refers to the previous preparation process and has made some modifications [32].

Scheme 1 Schematic principle of fluorescence/scattered light system based on WS$_2$ QDs-MnO$_2$ for GSH ratiometric detection
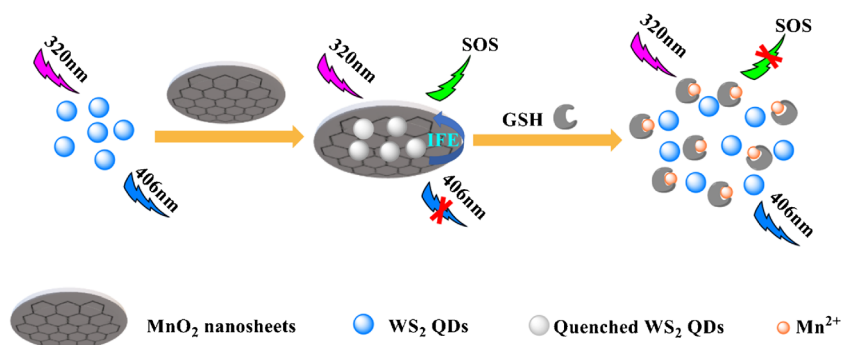
Fig. 1 **a** TEM image of WS$_2$ QDs(inset) corresponding size distribution histogram of WS$_2$ QDs. **b** FTIR spectrum of WS$_2$ QDs. **c** XRD spectrum of WS$_2$ QDs. **d** XPS spectrum of WS$_2$ QDs. **e** UV-Vis absorption and fluorescence spectrum of WS$_2$ QDs. **f** Excitation-dependent fluorescence emission spectra of WS$_2$ QDs, whereas inset shows the blue emission of WS$_2$ QDs under 365-nm excitation
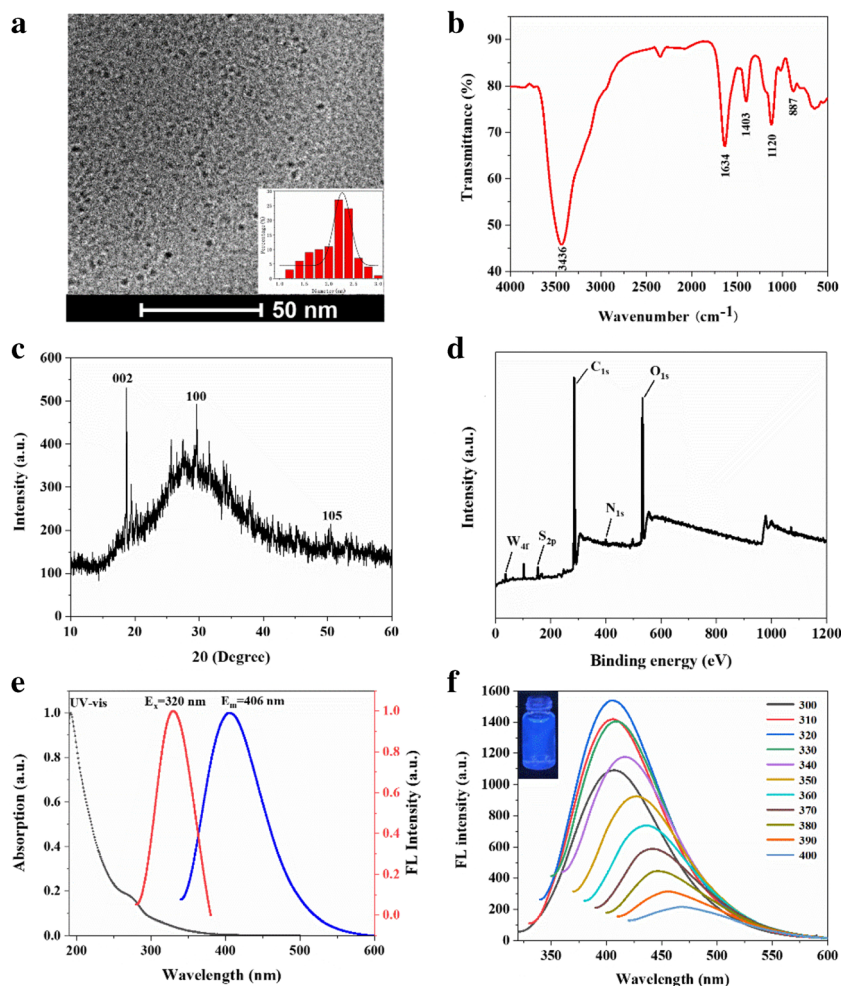
A total of 0.06 g of sodium tungstate was dissolved in 20 mL of water, adjusted to pH = 6.5 with 0.1 mol L^{-1} HCl, and 5 mL of a 100-mg mL^{-1} Cys aqueous solution was added. Ultrasonication for 5 min to make it evenly mixed. Then, the mixture was transferred into a 50-mL poly(tetrafluoroethylene) autoclave and reacted at 220 °C for 24 h. The product was slowly cooled to room temperature, centrifuged at 10,000 rpm for 30 min to remove large particles, and the supernatant was collected. Finally, the supernatant was dialyzing in a 1000 Da dialysis bag to remove unreacted material to obtain a WS$_2$ QDs solution.

Preparation of MnO$_2$ nanosheets

MnO$_2$ nanosheets were synthesized by the previously reported method and some modifications were made [33]. In detail, 3.5 mL of ethanol (99%), 3 mL of SDBS (0.5 mol L^{-1}), 0.25 mL of H$_2$SO$_4$ solution (0.1 mol L^{-1}), and 25 mL of distilled water were mixed together; then, the solution was heated to 95 °C. Slowly add 2 mL of KMnO$_4$ solution (0.05 mol L^{-1}) to the above solution and continue stirring for 40 min. After

cooling to room temperature, MnO$_2$ nanosheets were collected by centrifugation and repeatedly washed with distilled water for purification. Finally, the prepared MnO$_2$ nanosheets were freeze-dried into a brown-black powder. MnO$_2$ powder was dispersed in distilled water (0.4 mg mL^{-1}) to obtain a MnO$_2$ nanosheet solution.

Quantum yield measurements

The ratio of the fluorescence intensity to the absorbed light intensity of WS$_2$ QDs determines its quantum yield (QY). Absolute QY measurements were taken in a FLS920 spectrometer equipped with a calibrated integrating sphere. The cuvette containing the WS$_2$ QDs aqueous solution was placed in an integrating sphere to measure its QY, and the solvent water was used as a blank sample for reference measurement.

The detection of GSH with WS$_2$ QDs-MnO$_2$ system

First, 100.0 μL of WS$_2$ QDs and 300.0 μL MnO$_2$ solution were placed in a 10-mL volumetric flask, and then, different

Fig. 2 **a** TEM image of MnO_2 nanosheets. **b** UV-Vis absorption of MnO_2 nanosheets. **c** FTIR spectrum of MnO_2 nanosheets. **d** XPS spectrum of Mn_{2p} in MnO_2 nanosheets
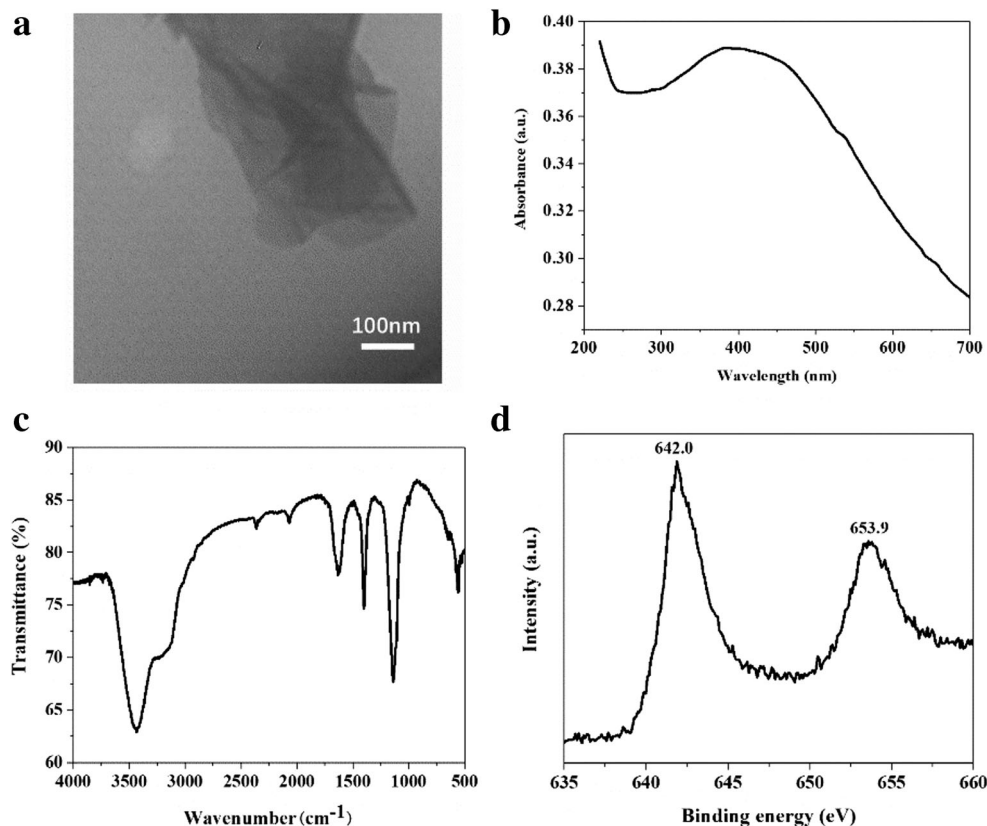
concentrations of GSH solution (2 mM) were added. The mixture was diluted to 10.0 mL with HEPES buffer at pH = 7. Whereafter, the mixture was incubated at room temperature for 30 min. Finally, the fluorescence emission spectrum was recorded using 320-nm excitation wavelength (5/5 nm slit width).

Results and discussion

Characterizations of WS₂ QDs and MnO₂ nanosheets

The characteristics of WS_2 QDs were analyzed by TEM, FT-IR, XRD, XPS, and fluorescence spectra. Figure 1 a shows the

TEM image and particle size distribution of WS_2 QDs. It can be seen that WS_2 QDs were quasi-spherical and monodisperse, with an average particle size of about 2.3 nm. The FTIR spectrum of WS_2 QDs is shown in Fig. 1b. The bending vibration peak of C–H is at 890 cm^{-1}, the stretching vibration peak of C–O is at 1120 cm^{-1}, and the peaks at 1634 cm^{-1} and 1403 cm^{-1} are associated to the stretching vibration of C=O and C–N of amide bond. At 3436 cm^{-1}, there are N–H/O–H stretching vibration peaks. The above results indicate that –OH, –NH₂, and –COOH exist on the surface of WS_2 QDs. Figure 1 c shows that WS_2 QDs have characteristic XRD peaks at $2\theta = 18.5°$, 29.6°, and 50.3°, which correspond to the diffraction peaks of the (002), (100), and (105) lattice
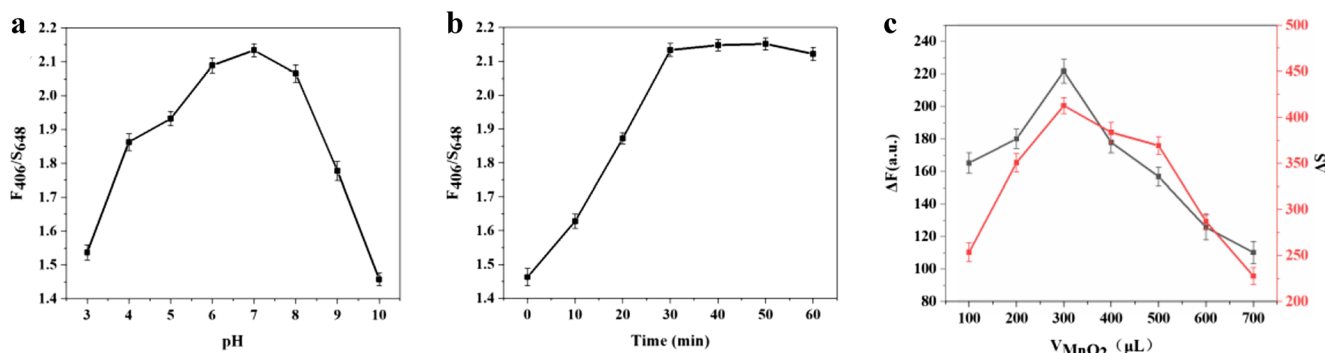
Fig. 3 **a** Effects of pH to the value of F_{406}/S_{648}. Conditions: MnO_2 nanosheets, 300.0 μL; GSH, 60.0 μM; 25 °C for 30 min. **b** Effects of reaction time to the value of F_{406}/S_{648}. Conditions: MnO_2 nanosheets, 300.0 μL; GSH, 60.0 μM; pH = 7.0; 25 °C. **c** Effects of MnO_2 volume to ΔF (black) and ΔS (red). Conditions: GSH, 60.0 μM; pH = 7.0; 25 °C for 30 min. Error bars are the standard deviation of three independent experiments

Fig. 4 **a** Fluorescence and SOS spectra of WS$_2$ QDs-MnO$_2$ (black), WS$_2$ QDs-MnO$_2$ + GSH (red) and WS$_2$ QDs (blue). **b** UV-Vis absorption spectra of WS$_2$ QDs, MnO$_2$, and WS$_2$ QDs-MnO$_2$. **c** Excitations and emission spectra of WS$_2$ QDs; UV-Vis absorption spectra of MnO$_2$ nanosheets without or with GSH. **d** Fluorescence decay curves of WS$_2$ QDs before and after the addition of MnO$_2$ nanosheets
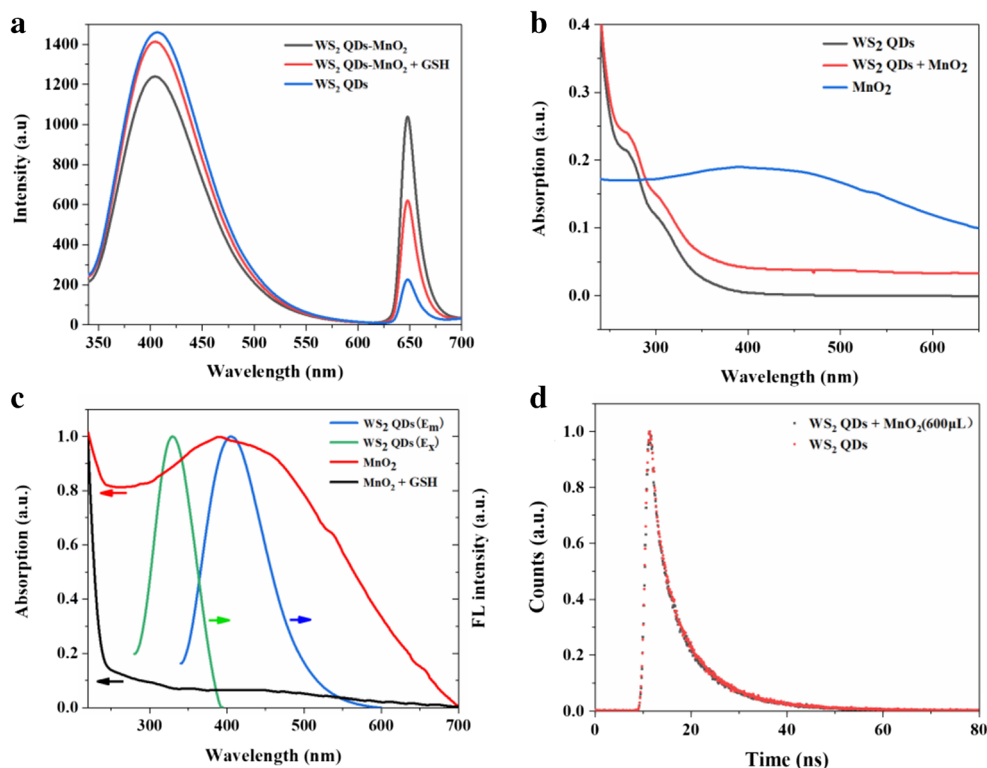
planes of WS$_2$ reported in the literature. The XPS method was used to study the surface element composition. As shown in Fig. 1d, the surface of WS$_2$ QDs contains carbon (C), nitrogen (N), oxygen (O), sulfur (S), and tungsten (W) elements. Figure 1 e shows the UV-Vis absorption spectra and fluorescence spectrum of WS$_2$ QDs. The optimal excitation and emission wavelengths of WS$_2$ QDs are 320 and 406 nm, respectively. The WS$_2$ QDs solution is colorless under white light and emits bright blue light under 365 nm UV light (Fig. 1f illustration). The fluorescence emission wavelength changes with the excitation wavelength, indicating that the emission spectrum of WS$_2$ QDs is affected by the excitation light. The measured QY of WS$_2$ QDs aqueous solution was 10.1%, which was higher than the QY of WS$_2$ QDs prepared by other methods.

The characterizations of MnO$_2$ nanosheets were investigated by TEM, UV-Vis, FT-IR, and XRD spectra. TEM microscopy (Fig. 2a) showed that the MnO$_2$ nanosheets had a uniform plate-like structure with occasional folds and crinkles, with an average size of about 300 nm. In addition, as shown in Fig. 2b, the UV-Vis absorption spectrum of the MnO$_2$ nanosheets shows a broad absorption peak in the range of 250 nm to 600 nm, and 380 nm is its characteristic absorption peak. As shown in Fig. 2c, the characteristic peak at 558 cm^{-1} in the FTIR spectrum of the MnO$_2$ nanosheets is due to the tensile vibration of Mn-O. The XPS spectrum of MnO$_2$ nanosheets is shown in Fig. S1. The XPS spectrum of Mn$_{2p}$ (Fig. 2d) shows two peaks at 642.0 and 653.9 eV, corresponding to Mn$_{2p3/2}$ and Mn$_{2p1/2}$ of MnO$_2$, respectively, which are consistent with

Fig. 5 **a** Fluorescence and SOS spectra of WS$_2$ QDs-MnO$_2$ system at different GSH (0–60 μM) concentrations under 320-nm excitation wavelength. **b** The linear relationship of F$_{406}$/S$_{648}$ versus different concentrations of GSH (0–60 μM)
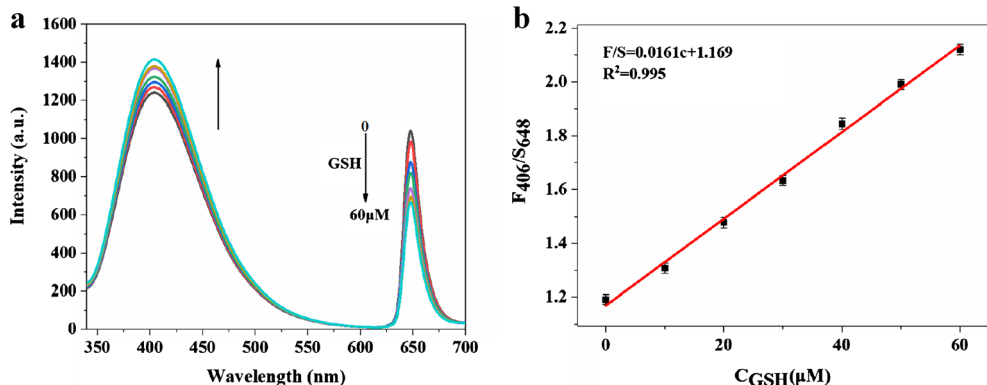
Table 1 Comparison of reported methods with current work for GSH detection

Methods	Probes	Detection limit (μM)	Detection range (μM)	References
Fluorimetry	g-C$_3$N$_4$-MnO$_2$	0–2000	0.2	[35]
Fluorimetry	CDs-MnO$_2$	1–10	0.3	[36]
Fluorimetry	AuNC@BSA-MnO$_2$	0–500	20	[37]
Fluorimetry	GQDs-MnO$_2$	0.5–10	150	[38]
Fluorimetry	Au(III)/CDC	0–150	2.02	[39]
Fluorimetry	CDs-Br	0–34	0.14	[40]
Fluorimetry	BNQDs-MnO$_2$	0.5–250	0.16	[34]
Fluorimetry	CPs@MnO$_2$-AgNPs	0.8–80	0.55	[41]
Fluorimetry	CDs@Ag(I)	10–10	0.38	[42]
Colorimetric	CDs	0–7	0.3	[43]
Colorimetric	3,3′,5,5′-tetramethylbenzidine	1–25	300	[44]
Fluorimetry and SOS	WS$_2$ QDs-MnO$_2$	0–60	0.12	This work

those reported in the previous literature [34]. The above results indicate the successful formation of MnO$_2$ nanosheets.

Optimization of experimental conditions

In order to develop a colorimetric assay for GSH detection with excellent performance, experimental conditions such as pH, incubation time, and volume of MnO$_2$ nanosheets were optimized.

As shown in Fig. 3a, the F$_{406}$/S$_{648}$ values (F$_{406}$ and S$_{648}$ are the fluorescence of WS$_2$ QDs at 406 nm and the SOS of system at 648 nm, respectively) are gradually increasing in the pH range of 3.0 to 7.0. Then, as the pH (7.0–10.0) increases, F$_{406}$/S$_{648}$ gradually decreases. The maximum is reached at pH = 7.0. In view of the above results, HEPBS buffer (10 mM) having a pH of 7.0 was selected as the working pH of the GSH assay. As shown in Fig. 3b, when GSH was added to the WS$_2$ QDs-MnO$_2$ system, the F$_{406}$/S$_{648}$ value increased as the reaction time increased from 0 to 30 min. However, when the reaction time exceeded 30 min, F$_{406}$/S$_{648}$ showed almost no change. Therefore, 30 min was selected for further sensitive detection of GSH in further

experiments. The volume of MnO$_2$ nanosheets has a great impact on the sensitivity and linear range of GSH detection. As shown in Fig. 3c, as MnO$_2$ was added from 100.0 to 300.0 μL, ΔF (black) and ΔS (red) increased rapidly. ΔF is the change in fluorescence intensity of WS$_2$ QDs at 406 nm in the WS$_2$ QDs-MnO$_2$ system with and without GSH. ΔS is the change in the fluorescence intensity of SOS at 648 nm in the WS$_2$ QDs-MnO$_2$ system with and without GSH. As the volume of MnO$_2$ increases further, they gradually decrease. Therefore, 300.0 μL of MnO$_2$ nanosheets was used as the optimum conditions for subsequent experiments. The fluorescence and SOS spectra of the system at different pH, reaction time, and MnO$_2$ volume are shown in Figs. S2a, S2b, and S2c, respectively.

Detection strategy and mechanism discussion of GSH

As shown in Fig. 4a, due to the small size of the WS$_2$ QDs, the WS$_2$ QDs that exist alone have only weak SOS signals. In addition, the strength of F$_{406}$ and S$_{648}$ was relatively close before GSH was added to the WS$_2$ QDs-MnO$_2$ system. However, when GSH was added, F$_{406}$ increased and S$_{648}$

Table 2 Recovery test results of GSH detection in tap water and pool water samples

Samples	Added (μM)	Measured (μM)	Recover (%)	RSD* (%, $n = 3$)
Tap water	10	10.41	104.1	2.29
	20	19.35	96.75	2.71
	30	29.61	98.70	3.15
Lake water	10	9.53	95.3	2.69
	20	20.42	102.1	2.54
	30	30.29	100.97	3.37

Table 3 Recovery test results of GSH detection in human serum samples

Samples	Added (μM)	Measured (μM)	Recovery (%)	RSD* (%, $n = 3$)
Sample 1	10	10.43	104.3	2.92
	20	19.45	97.25	3.16
	30	30.51	101.7	3.68
Sample 2	10	9.56	95.6	2.79
	20	20.59	102.95	3.85
	30	30.41	101.37	4.01

decreased. Therefore, the above phenomenon indicates that the ratio sensing platform can be used for GSH detection.

Next, the mechanism of fluorescence quenching of WS$_2$ QDs by MnO$_2$ nanosheets was studied. Figure 4 b shows the UV-visible absorption spectra of WS$_2$ QDs, MnO$_2$, and WS$_2$ QDs-MnO$_2$. Compared with the absorption spectrum of WS$_2$ QDs alone, there is no new absorption peak after the addition of MnO$_2$, indicating that no non-luminous ground state complex is formed between WS$_2$ QDs and MnO$_2$. So, the static quenching mechanism is excluded. As shown in Fig. 4c, the excitation and emission spectra of WS$_2$ QDs overlap with the UV-visible absorption spectrum of MnO$_2$. Based on the above results, fluorescence resonance energy transfer (FRET) or IFE may occur. In addition, in the absence of MnO$_2$, the fluorescence lifetime of WS$_2$ QDs is 6.16 ns, and the fluorescence lifetime (5.93 ns) hardly changes after adding MnO$_2$, as shown in Fig. 4d and supporting information Table S1. Therefore, the FRET mechanism is excluded from the fluorescence lifetime data, and the results indicate that IFE is the quenching mechanism of WS$_2$ QDs.

GSH has a strong reducing ability. When GSH is added to the WS2 QDs-MnO$_2$ system, GSH reduces MnO$_2$ to Mn^{2+}, resulting in dissociation of MnO$_2$ nanosheets, as shown in the equation 1. At the same time, the disappearance of the characteristic absorption band of MnO$_2$ (Fig. 4c) inhibited the IFE to WS$_2$ QDs, resulting in the fluorescence recovery of WS$_2$ QDs. The reduction in size of MnO$_2$ nanosheets after being decomposed by GSH results in a decrease in the SOS of the system. Therefore, the ratio detection of GSH was obtained by the fluorescence and SOS dual signal response.

$$2GSH + MnO_2 + 2H^+ \rightarrow GSSG + Mn^{2+} + H_2O \qquad (1)$$

Ratiometric detection of GSH

In order to prove the applicability of this ratio sensing platform for GSH detection, we investigated the response of the WS$_2$ QDs-MnO$_2$ system to GSH. As shown in Fig. 5a, under the optimal experimental conditions, as GSH concentration increased, F$_{406}$ increased, and S$_{648}$ decreased. At the same time, a good linear relationship was obtained over a concentration

range of 0 to 60 μM with a correlation coefficient of 0.995 (Fig. 3b). The linear equation is F$_{406}$/S$_{648}$ = 0.0161c + 1.169. The LOD is 0.12 μM. In addition, our sensing platform was compared with previously reported strategies for GSH detection (Table 1). The results show that our sensing platform has high sensitivity, wide linear range, and low detection limit. Therefore, the WS$_2$ QDs-MnO$_2$ system shows the potential advantages of determining GSH in actual samples.

The selectivity of GSH detection

Selectivity is an important parameter for studying the performance of fluorescence sensing platforms. In order to evaluate the selectivity of the WS$_2$ QDs-MnO$_2$ system for GSH, the fluorescence responses of WS$_2$ QDs-MnO$_2$ to some metal ions (Na$^+$, K$^+$, Mg^{2+}, Ca^{2+}, Fe^{3+}, and Zn^{2+}), amino acids (Hcy, Cys, Ser, Tyr, Gly, and His), and biomolecules (glucose, galactose, and BSA) were investigated. As shown in Fig. S3, after adding the above interfering substances with the same concentration as GSH (60 μM), the F$_{406}$/S$_{648}$ value of the WS$_2$ QDs-MnO$_2$ system was basically unchanged. When GSH was added, the F$_{406}$/S$_{648}$ value showed a significant change. Although AA as a reducing agent will cause the F$_{406}$/S$_{648}$ value of the system to fluctuate, the concentration of GSH in plasma is much larger than AA, so the effect of AA on the determination of GSH can be ignored. These results show that the WS$_2$ QDs-MnO$_2$ system has good selectivity and competitiveness for the detection of GSH.

Detection of GSH in real samples

In order to evaluate the reliability and applicability of the WS$_2$ QDs-MnO$_2$ system in practical applications, spiked recovery experiments were performed to determine the GSH levels in two actual water samples (tap water and lake water) and human serum. First, the real water sample was filtered through a 0.45 μm membrane to remove large suspended particles, and then, different concentrations of GSH (10, 20, and 30 μM) were added. The WS$_2$ QDs-MnO$_2$ system was used to detect the concentration of GSH in the real water sample after spiking, and each

concentration was measured three times. The collected serum sample was centrifuged at 10,000 rpm, and the light yellow supernatant was taken. Because the concentration of GSH in human serum was as high as mM, the supernatant was diluted 50 times with ultrapure water so that the original GSH concentration could fall into the standard calibration curve of this method, and then, the GSH spike recovery experiment was the same. Without spiking, the GSH concentration in the diluted serum sample was 0.56 μM. Tables 2 and 3 list the corresponding analysis results before and after adding GSH to actual water samples and human serum. When we use this platform for determination, the recovery of quantitatively spiked GSH in actual water samples is 95.3–104.1%, and the relative standard deviation (RSD) is 2.29–3.37%. The recovery of GSH in human serum was 95.6–104.3%, and the RSD was 2.79–4.01%. Therefore, the proposed WS_2 QDs-MnO_2 nanoprobe for detecting GSH in actual water and serum samples is feasible and reliable.

Conclusion

In summary, we have successfully designed a new GSH ratio detection method based on the fluorescence and SOS of the WS_2 QDs-MnO_2 system. This method has the advantages of simplicity, low cost, wide linear range, high sensitivity, environmental friendliness, and good selectivity. With the addition of large-sized MnO_2 nanosheets, the fluorescence of WS_2 QDs was quenched by IFE, and the SOS of the scatterer was enhanced to be relatively close to fluorescence. As GSH was gradually added to the WS_2 QDs-MnO_2 system, GSH reduced the MnO_2 nanosheets to Mn^{2+}, which led to the fluorescence recovery of WS_2 QDs and the decrease of SOS of the scatterers. In the concentration range of 0 to 60 μM, the value of F_{406}/S_{648} increased linearly with the increase of GSH, and the LOD was calculated to be 0.12 μM. It is worth noting that the proportional system has been successfully applied to the detection of GSH in actual samples. We believe that the proportional system will have great application potential in the fields of environmental monitoring. This newly proposed ratio detection method provides a new perspective for the construction of new biosensing.

Compliance with ethical standards

Conflict of interest The authors declare that they have no competing interests.

References

1. Li S, Wang L, Zhang X, Chai H, Huang Y (2018) A Co, N co-doped hierarchically porous carbon hybrid as a highly efficient oxidase mimetic for glutathione detection. Sensors and Actuators B: Chemical

2. Li J, Rao X, Xiang F, Wei J, Yuan M, Liu Z (2018) A photoluminescence "switch-on" nanosensor composed of nitrogen and sulphur co-doped carbon dots and gold nanoparticles for discriminative detection of glutathione. Analyst 143(9):2083–2089

3. Han L, Liu SG, Zhang XF, Tao BX, Li NB, Luo HQ (2018) A sensitive polymer dots-manganese dioxide fluorescent nanosensor for "turn-on" detection of glutathione in human serum. Sensors Actuators B Chem 258:25–31

4. Gao Y, Wu K, Li H, Chen W, Fu M, Yue K, Zhu X, Liu Q (2018) Glutathione detection based on peroxidase-like activity of Co3O4–Montmorillonite nanocomposites. Sensors Actuators B Chem 273:1635–1639

5. Yan F, Bai Z, Zu F, Zhang Y, Sun X, Ma T, Chen L (2019) Yellow-emissive carbon dots with a large stokes shift are viable fluorescent probes for detection and cellular imaging of silver ions and glutathione. Mikrochim Acta 186(2):113

6. Yang X-F, Huang Q, Zhong Y, Li Z, Li H, Lowry M, Escobedo JO, Strongin RM (2014) A dual emission fluorescent probe enables simultaneous detection of glutathione and cysteine/homocysteine. Chem Sci 5(6):2177–2183

7. He L, Xu Q, Liu Y, Wei H, Tang Y, Lin W (2015) Coumarin-based turn-on fluorescence probe for specific detection of glutathione over cysteine and homocysteine. ACS Appl Mater Interfaces 7(23):12809–12813

8. Huang Y, Zhou J, Feng H, Zheng J, Ma H-M, Liu W, Tang C, Ao H, Zhao M, Qian Z (2016) A dual-channel fluorescent chemosensor for discriminative detection of glutathione based on functionalized carbon quantum dots. Biosens Bioelectron 86:748–755

9. Lee PT, Goncalves LM, Compton RG (2015) Electrochemical determination of free and total glutathione in human saliva samples. Sensors Actuators B Chem 221:962–968

10. Ge J, Cai R, Chen X, Wu Q, Zhang L, Jiang Y, Cui C, Wan S, Tan W (2019) Facile approach to prepare HSA-templated MnO2 nanosheets as oxidase mimic for colorimetric detection of glutathione. Talanta 195:40–45

11. Ouyang L, Zhu L, Jiang J, Tang H (2014) A surface-enhanced Raman scattering method for detection of trace glutathione on the basis of immobilized silver nanoparticles and crystal violet probe. Anal Chim Acta 816:41–49

12. Bigdeli A, Ghasemi F, Abbasi-Moayed S, Shahrajabian M, Fahimi-Kashani N, Jafarinejad S, Farahmand Nejad MA, Hormozi-Nezhad MR (2019) Ratiometric fluorescent nanoprobes for visual detection: design principles and recent advances - a review. Anal Chim Acta 1079:30–58

13. Ma Z, Wu T, Li P, Liu M, Huang S, Li H, Zhang Y, Yao S (2019) A dual (colorimetric and fluorometric) detection scheme for glutathione and silver (I) based on the oxidase mimicking activity of MnO2 nanosheets. Mikrochim Acta 186(8):498

14. Xu X, He L, Long Y, Pan S, Liu H, Yang J, Hu X (2019) S-doped carbon dots capped ZnCdTe quantum dots for ratiometric fluorescence sensing of guanine. Sensors Actuators B Chem 279:44–52

15. Chen S, Jia Y, Zou GY, Yu YL, Wang JH (2019) A ratiometric fluorescent nanoprobe based on naphthalimide derivative-functionalized carbon dots for imaging lysosomal formaldehyde in HeLa cells. Nanoscale 11(13):6377–6383

16. Yan F, Zu F, Xu J, Zhou X, Bai Z, Ma C, Luo Y, Chen L (2019) Fluorescent carbon dots for ratiometric detection of curcumin and ferric ion based on inner filter effect, cell imaging and PVDF membrane fouling research of iron flocculants in wastewater treatment. Sensors Actuators B Chem 287:231–240

17. Jin H, Baek B, Kim D, Wu F, Batteas JD, Cheon J, Son DH (2017) Effects of direct solvent-quantum dot interaction on the optical properties of colloidal monolayer WS2 quantum dots. Nano Lett 17(12):7471–7477

18. Cheng G, Li B, Zhao C, Yan X, Wang H, Lau KM, Wang J (2018) Interfacially bound exciton state in a hybrid structure of monolayer WS2 and InGaN quantum dots. Nano Lett 18(9):5640–5645

19. Srivastava M, Tiwari P, Mall VK, Srivastava SK, Prakash R (2019) Voltammetric determination of the antimalarial drug chloroquine using a glassy carbon electrode modified with reduced graphene oxide on WS2 quantum dots. Microchim Acta 186(7):415

20. Fang Y, Pan J, Zhang D, Wang D, Hirose HT, Terashima T, Uji S, Yuan Y, Li W, Tian Z, Xue J, Ma Y, Zhao W, Xue Q, Mu G, Zhang H, Huang F (2019) Discovery of superconductivity in 2M WS2 with possible topological surface states. Adv Mater 31(30): e1901942

21. Dhenadhayalan N, Lin KC, Saleh TA (2019) Recent advances in functionalized carbon dots toward the design of efficient materials for sensing and catalysis applications. Small:e1905767

22. Chen J, Meng H, Tian Y, Yang R, Du D, Li Z, Qu L, Lin Y (2019) Recent advances in functionalized MnO2 nanosheets for biosensing and biomedicine applications. Nanoscale Horizons 4(2):321–338

23. Liu Z, Zhang S, Lin H, Zhao M, Yao H, Zhang L, Peng W, Chen Y (2018) Theranostic 2D ultrathin MnO2 nanosheets with fast responsibility to endogenous tumor microenvironment and exogenous NIR irradiation. Biomaterials 155:54–63

24. Zhu S, Wang S, Xia M, Wang B, Huang Y, Zhang D, Zhang X, Wang G (2019) Intracellular imaging of glutathione with MnO2 Nanosheet@Ru(bpy)32+–UiO-66 nanocomposites. ACS Appl Mater Interfaces 11(35):31693–31699

25. Xiao T, Sun J, Zhao J, Wang S, Liu G, Yang X (2018) FRET effect between fluorescent polydopamine nanoparticles and MnO2 nanosheets and its application for sensitive sensing of alkaline phosphatase. ACS Appl Mater Interfaces 10(7):6560–6569

26. Yan X, Song Y, Zhu C, Li H, Du D, Su X, Lin Y (2018) MnO2 nanosheet-carbon dots sensing platform for sensitive detection of organophosphorus pesticides. Anal Chem 90(4):2618–2624

27. Liu Y, Zeng Z, Bloom B, Waldeck DH, Wei J (2018) Stable low-current electrodeposition of α-MnO2 on superaligned electrospun carbon nanofibers for high-performance energy storage. Small 14(3):1703237

28. Thakkar D, Gevriya B, Mashru RC (2014) Study on interaction between palladium(capital I, Ukrainiancapital I, Ukrainian)-linezolid chelate with eosin by resonance Rayleigh scattering, second order of scattering and frequency doubling scattering methods using Taguchi orthogonal array design. Spectrochim Acta A Mol Biomol Spectrosc 122:75–81

29. Chen P, Liu S, Liu Z, Hu X (2011) Study on the ternary mixed ligand complex of palladium(II)-aminophylline-fluorescein sodium by resonance Rayleigh scattering, second-order scattering and frequency doubling scattering spectrum and its analytical application. Spectrochim Acta A Mol Biomol Spectrosc 78(1):518–522

30. Yan F, Sun Z, Ma T, Sun X, Xu J, Wang R, Chen L (2019) Ratiometric fluorescent nanoprobes based on resonance Rayleigh scattering and inner filter effect for detecting alizarin red and Pb2+. Spectrochimica Acta Part A: Molecular and Biomolecular Spectroscopy:117843

31. Wu Z, Nan D, Yang H, Pan S, Liu H, Hu X (2019) A ratiometric fluorescence-scattered light strategy based on MoS2 quantum dots/ CoOOH nanoflakes system for ascorbic acid detection. Anal Chim Acta 1091:59–68

32. Singh VK, Yadav MS, Mishra H, Kumar R, Tiwari RS, Pandey A, Srivastava A (2019) WS2 quantum dot graphene nanocomposite film for UV photodetection. ACS Applied Nano Materials 2(6): 3934–3942

33. Zhu Z, Lin X, Wu L, Zhao C, Zheng Y, Liu A, Lin L, Lin X (2018) "Switch-on" fluorescent nanosensor based on nitrogen-doped carbon dots-MnO2 nanocomposites for probing the activity of acid phosphatase. Sensors Actuators B Chem 274:609–615

34. Peng C, Xing H, Fan X, Xue Y, Li J, Wang E (2019) Glutathione regulated inner filter effect of MnO2 nanosheets on boron nitride quantum dots for sensitive assay. Anal Chem 91(9):5762–5767

35. Zhang XL, Zheng C, Guo SS, Li J, Yang HH, Chen G (2014) Turn-on fluorescence sensor for intracellular imaging of glutathione using g-C(3)N(4) nanosheet-MnO(2) sandwich nanocomposite. Anal Chem 86(7):3426–3434

36. Cai QY, Li J, Ge J, Zhang L, Hu YL, Li ZH, Qu LB (2015) A rapid fluorescence "switch-on" assay for glutathione detection by using carbon dots-MnO2 nanocomposites. Biosens Bioelectron 72:31–36

37. Lin S, Cheng H, Ouyang Q, Wei H (2016) Deciphering the quenching mechanism of 2D MnO2 nanosheets towards Au nanocluster fluorescence to design effective glutathione biosensors. Anal Methods 8(19):3935–3940

38. Yan X, Song Y, Zhu C, Song J, Du D, Su X, Lin Y (2016) Graphene quantum dot-MnO2 nanosheet based optical sensing platform: a sensitive fluorescence "turn off-on" nanosensor for glutathione detection and intracellular imaging. ACS Appl Mater Interfaces 8(34):21990–21996

39. Gu J, Hu D, Wang W, Zhang Q, Meng Z, Jia X, Xi K (2015) Carbon dot cluster as an efficient "off-on" fluorescent probe to detect Au(III) and glutathione. Biosens Bioelectron 68:27–33

40. Yan F, Ye Q, Xu J, He J, Chen L, Zhou X (2017) Carbon dots-bromoacetyl bromide conjugates as fluorescence probe for the detection of glutathione over cysteine and homocysteine. Sensors Actuators B Chem 251:753–762

41. Wang Q, Wang C, Wang X, Zhang Y, Wu Y, Dong C, Shuang S (2019) Construction of CPs@MnO2–AgNPs as a multifunctional nanosensor for glutathione sensing and cancer theranostics. Nanoscale 11(40):18845–18853

42. Jiao Y, Gao Y, Meng Y, Lu W, Liu Y, Han H, Shuang S, Li L, Dong C (2019) One-step synthesis of label-free Ratiometric fluorescence carbon dots for the detection of silver ions and glutathione and cellular imaging applications. ACS Appl Mater Interfaces 11(18):16822–16829

43. Shamsipur M, Safavi A, Mohammadpour Z (2014) Indirect colorimetric detection of glutathione based on its radical restoration ability using carbon nanodots as nanozymes. Sensors Actuators B Chem 199:463–469

44. Liu J, Meng L, Fei Z, Dyson PJ, Jing X, Liu X (2017) MnO2 nanosheets as an artificial enzyme to mimic oxidase for rapid and sensitive detection of glutathione. Biosens Bioelectron 90:69–74